Monitoring the Monthly Expansion Pattern of Pioneer Vegetation in Tidal Flats Using a Terrestrial Laser Scanner

Zhan, Yujian; Aarninkhof, Stefan G.J.; Wang, Zhengbing; Zhou, Yunxuan

BioOne COMPLETE

Monitoring the Monthly Expansion Pattern of Pioneer Vegetation in Tidal Flats Using a Terrestrial Laser Scanner

Authors: Zhan, Yujian, Aarninkhof, Stefan G.J., Wang, Zhengbing, and Zhou, Yunxuan

Monitoring the Monthly Expansion Pattern of Pioneer Vegetation in Tidal Flats Using a Terrestrial Laser Scanner

Yujian Zhan[†‡], Stefan G.J. Aarninkhof[‡], Zhengbing Wang[‡], and Yunxuan Zhou[†]*

[†]State Key Laboratory of Estuarine and Coastal Research
East China Normal University
Shanghai 200062, China

[‡]Faculty of Civil Engineering and Geosciences
Delft University of Technology
Delft 2628CN, The Netherlands

ABSTRACT

Zhan, Y.; Aarninkhof, S.G.J.; Wang, Z., and Zhou, Y., 2022. Monitoring the monthly expansion pattern of pioneer vegetation in tidal flats using a terrestrial laser scanner. *Journal of Coastal Research,* 38(3), 538–547. Coconut Creek (Florida), ISSN 0749-0208.

Research on the expansion pattern of pioneer vegetation in tidal flats is important, because this pattern affects the development of both topography and ecology. This study aimed to determine the monthly expansion patterns of seedlings and tussocks by using terrestrial laser scanning (TLS). Overall change process research and spatial analyses of both seedling recruitment and tussock development were carried out in this work. The results show that the overall change in pioneer vegetation reflected an expansion toward the shoreline in the first year and then a northward colonization in the second year. Moreover, positive feedback effects were observed between vegetation colonization and sedimentation accretion. Colonization accelerated the depositional process at the study site. Moreover, sedimentation accretion in the northern subarea, which is located close to the seawall, promoted the colonization of vegetation in this region. A strong spatial relationship was observed between seedling recruitment and tussock development. Tussocks tended to force seedlings to expand outward by squeezing the established space of the seedlings. Moreover, seedlings were densely concentrated within a certain distance from tussocks. The distances between seedlings and tussocks tended to shorten annually as the entire vegetation area underwent the expansion process. The average distance between seedlings was found to be concentrated from 10 to 20 m. The monthly vegetation expansion process was studied on small and medium scales in this work, revealing the advantages of TLS technology in rapidly acquiring data with high resolution and high precision.

ADDITIONAL INDEX WORDS: *Monthly monitoring, seedling and tussock.*

INTRODUCTION

Coastal zones colonized by salt marsh vegetation are among the most productive ecosystems in the world (Duarte, Middelburg, and Caraco, 2005). These areas are highly valued for their numerous ecosystem services (Zedler and Kercher, 2005). When pioneer species colonize a bare tidal flat, their seeds can develop into discrete circular, domed tussocks separated by open mudflats through clonal growth (Balke *et al.*, 2012; Hulzen and Bouma, 2007), and these discrete tussocks may eventually coalesce into continuous swards (Nehring and Hesse, 2008; Zhu *et al.*, 2012). However, salt marshes are vulnerable to natural and anthropogenic interference factors, including rigorous hydrological conditions, sediment availability, wetland reclamation, and sea-level rise (Ferronato *et al.*, 2018; Kirwan and Megonigal, 2013). Moreover, salt marshes frequently expand and retreat in response to external forces, such as wind waves, tidal flushing, and sediment input (Fagherazzi *et al.*, 2012; Ganju *et al.*, 2017); the accretion or erosion of mudflats and the resilience of marsh species to geomorphological changes also affect the size of salt marshes (Bouma *et al.*, 2016; Chen and Temmerman, 2013). Elevational differences of less than 10 cm can result in significant differences in vegetation distribution patterns (Marani *et al.*,

2006; Silvestri, Marani, and Marani, 2003; Suchrow and Jensen, 2010). Therefore, sediment availability is one of the most important factors affecting vegetation establishment and marsh stability on tidal flats (Donatelli *et al.*, 2018; Ganju *et al.*, 2017).

Most previous studies that evaluated plant patterns in salt marshes typically depended on several spatially dispersed samples or transect samples collected in field surveys; this type of data collection is labor intensive, time consuming, and sometimes restricted by the difficulty of accessing muddy marshes (Silvestri, Marani, and Marani, 2003; Yuan and Zhang, 2008). Refinements in the use of remote sensing technology have enabled researchers to characterize both the marsh topography (Hladik, Schalles, and Alber, 2013; Lee and Yeh, 2009) and the spatial distribution of vegetation (Huang and Zhang, 2007; Sadro, Gastil-Buhl, and Melack, 2007) at the whole-marsh scale. However, these methods are limited by data resolution, accuracy, and surface elevation estimations and are thus not able to detect monthly change processes undergone by salt marsh vegetation.

As a relatively new technology, the terrestrial laser scanning (TLS) technique can acquire high-accuracy surface data over a large area; this technology has been used to monitor geomorphological changes in tidal flats over the past several years (Guarnieri *et al.*, 2009; Thiebes *et al.*, 2013; Xie *et al.*, 2017). Moreover, TLS has been used to detect seasonal vegetation and morphological changes in coastal salt marshes based on digital surface models and digital canopy models generated from TLS data (Xie *et al.*, 2021). However, few studies have used TLS to
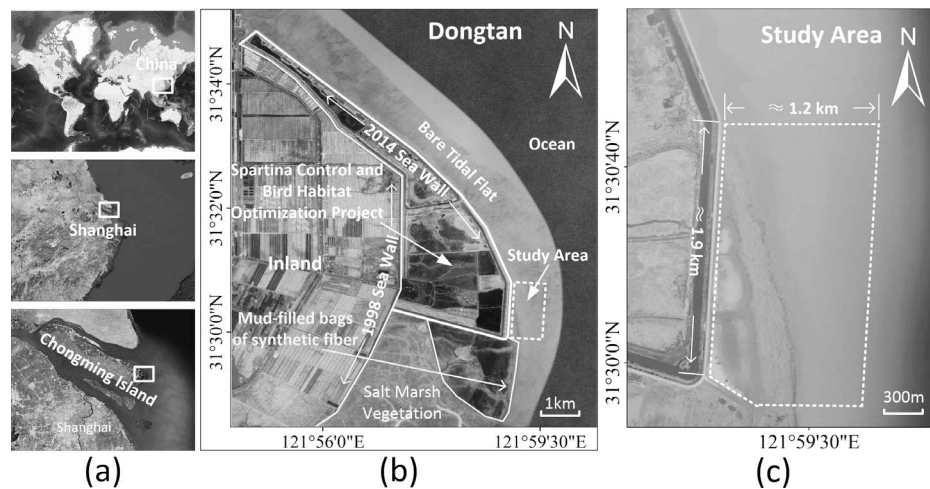
Figure 1. The location of the study area. (a) The location of Dongtan; (b) the boundaries of seawalls, projects, and land-use types; and (c) general information about the study area.

monitor monthly changes in salt marsh vegetation, especially during the expansion process of pioneer vegetation.

The objective of this work is to study the potential of using TLS techniques to monitor the monthly change pattern of pioneer vegetation in terms of seedling recruitment and tussock development. To meet this objective, vegetation and topographic point sets are extracted from TLS data, several features are quantified using these point sets, the monthly vegetation and topographic changes are presented and studied, and finally, statistical analyses are performed on both the seedling recruitment and the tussock development data and the results are discussed.

METHODS

In this section, the characteristics of the study area are described, followed by the schemes by which the TLS data are acquired and processed. Then, statistical and spatial analysis methods are designed and constructed to evaluate the change patterns of seedlings and tussocks.

Study Area

Dongtan, which is located at the eastern end of Chongming Island, is the largest muddy tidal flat in the Yangtze Estuary (Figure 1a). The tides in the Yangtze River delta are irregularly semidiurnal, with the ranges of two successive tides being unequal. In eastern Chongming, the tidal range is 2.5 m on average and approximately 3.5 m during spring tides; the highest astronomical tide is 5.2 m above the lowest astronomical tide, or 1 m higher than the mean spring high tide (recorded at the Sheshan Gauging station; Chen and Yang, 1988). Generally, in the Chongming Dongtan wetland, low-lying tidal flats are vegetated by the pioneering marsh species *Scirpus* spp. (mainly *Scirpus mariqueter, Scirpus triqueter,* and *Scirpus planiculmis*), and the highlands are characterized by *Phragmites australis* and *Spartina alterniflora* (Ge *et al.*, 2015).

To implement the Spartina Control and Bird Habitat Optimization Project, a 26.9-km-long seawall (the yellow solid line in Figure 1b) was constructed by the Chongming Dongtan National Nature Reserve to encompass a salt marsh area that was previously predominantly covered by *Spartina*. At the same time, the area south of the seawall was reclaimed by mud-filled synthetic fiber bags (Figure 1b).

From 2013 to 2015, almost all invasive *S. alterniflora* was eradicated based on the large restoration engineering project launched by the managers of the nature reserve (Hu *et al.*, 2015). The frontier tidal flat is dominated by native *Scirpus* spp.

The study area (Figure 1c) is an open salt marsh located in front of the seawall (31°28′28″ to approximately 31°35′11″ N, 121°54′31″ to approximately 122°00′22″ E) at its SE corner. The salt marsh is mainly vegetated by the pioneering marsh species *S. mariqueter* (Figure 2e), has an alongshore-direction length of nearly 1.9 km, and has a cross-shore-direction length within 1.2 km from the seawall (which is within the actual effective detection range of TLS).

Data Acquisition and Preprocessing

Ten field surveys (Table 1) were carried out from 2017 to 2018 to acquire LIDAR data in the study area (no vegetation was found in the surveys conducted before May in either year). The TLS instrument was set in a fixed scanning position (the yellow five-pointed star in Figure 2a) to cover the open salt marsh in the study area. During these 10 surveys (Table 1), TLS data were acquired by using a VZ-4000 terrestrial laser scanner from Riegl Laser Measurement Systems (Figure 2b) with an accuracy of 15 mm. The Riegl VZ-4000 instrument provides high-speed, noncontact data acquisition using a narrow infrared laser beam (at a wavelength of 1550 nm; Fey *et al.*, 2019) and a rapid-scanning mechanism. This scanner provides data at a measurement range of up to 4000 m and an efficient measurement rate of up to 122,000 measurements per second, with a wide field of view comprising 60° vertically and 360°
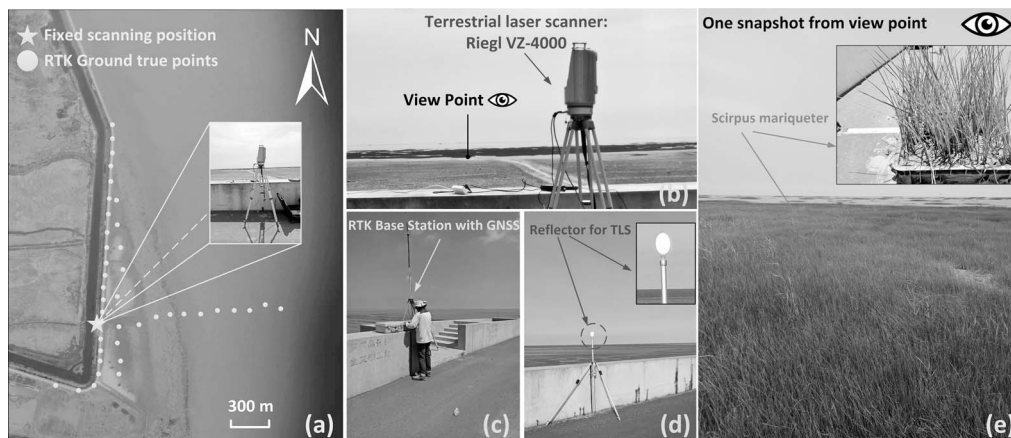
Figure 2. The scanning positions and applied instruments. (a) The fixed scanning position (star) and the RTK points (circles); (b) the Riegl VZ-4000 in the scanning position on the seawall; (c) one snapshot of the RTK base station with the global navigation satellite system; (d) one flat reflector on the seawall with a 5-cm diameter; and (e) one snapshot from the perspective of panel b.

horizontally. The scanning frequency was 30 Hz in this work; this frequency was the most powerful mode in which the TLS instrument could detect the maximum range of the studied tidal flat. The real-time kinematic (RTK) data collected in this work included the coordinates of the tops of all reflectors (Figure 2d) and the ground-truth points. The locations of both the base station and the receivers (Figure 2c) used to acquire these data were determined using an RTK GPS (Ashtech Corp.) based on the local Wusong bathymetric benchmark.

Preprocessing of the TLS data, including preliminary georeferencing, noise-point filtering, and selection of the study area, was carried out using RiSCAN Pro software (version 2.2.1) developed by Riegl. The raw TLS data (in the scanner's coordinate system), the point pairs, and the original transform matrixes were exported from the RiSCAN Pro software into ASCII files.

To verify the reliability of the point cloud data, the root-mean-square error (RMSE) was applied to calculate the vertical errors between the ground-truth RTK points and the corresponding points from the georeferenced LIDAR data.

Vegetation Extraction and Terrain Data Acquisition

Salt marsh vegetation was extracted from the georeferenced TLS data. Previous works provided a vegetation-filtering method (Guarnieri *et al.*, 2009) by using a moving window

with a given search size to obtain the lowest points and assuming these points were the ground points. The vegetation in this study area is low and dense, with an average height ranging from 10 to 20 cm. The used laser may not have been able to penetrate this vegetation (Lei *et al.*, 2014).

In this work, vegetation areas were first distinguished from the bare tidal flats. First, the TLS data resulting from each scan were clipped into several subbanded areas, with the long side oriented in the cross-shore direction. Then, the thickness of each point in each subbanded area was calculated by searching its neighboring points within a given radius. After that, these points were preliminarily classified into vegetation points and nonvegetation points based on the given threshold value (5 cm in this work). For each subbanded area, the nonvegetation points were spatially interpolated into grid points. Finally, the vertical distance between each vegetation point and its nearest grid point in the horizontal space was calculated. The vegetation points were again classified into vegetation points and nonvegetation points using a given vertical distance threshold value. Thus, the nonvegetation points resulting from these two classification steps were merged into ground points (the gray points in Figure 3). All these data were processed using the Point Cloud Library (an open-source, third-party library) and Cloud Compare software (an efficient open-source tool).

With these ground points, terrain datasets could be generated for further research. The points were first converted into PCD files (a standard format supported by Cloud Compare software) for each month. Then, the boundaries (2D polygon) of all PCD files were extracted with a given spatial resolution (30 m). Subsequently, the merged data were clipped by their minimum outer boundary based on these extracted boundaries and resampled from the pregenerated grids at a spatial resolution of 10 m. Two digital elevation models (DEMs) of the deposition rate were obtained by subtracting the resampled PCD files of the first and the last months and dividing the difference by the time span. Areas with different depositional

Table 1. *The attributes of all LIDAR data.*

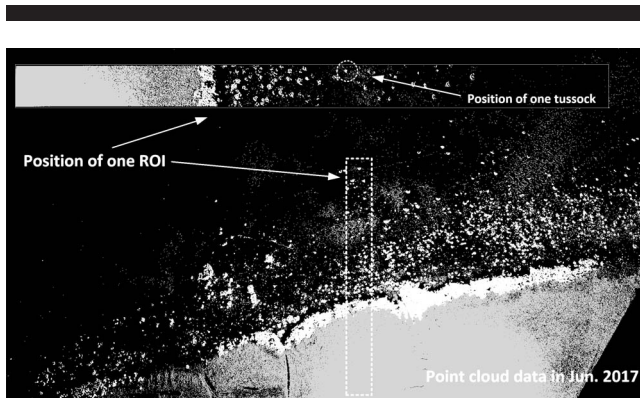| Survey	Date	Resolution (m²)	Scan Radius (m)	Survey Area (ha)
S1	11 May 2017	0.01–159.36	2883	1866.75
S2	12 June 2017	0.01–673.97	4787	4618.92
S3	3 July 2017	0.01–694.37	4578	3349.06
S4	18 August 2017	0.01–727.00	4666	4907.28
S5	29 September 2017	0.01–2098.55	4297	2677.87
S6	13 May 2018	0.01–275.92	5034	3975.02
S7	1 June 2018	0.01–569.72	5072	5820.52
S8	10 July 2018	0.01–1547.00	5150	3743.7
S9	15 August 2018	0.01–279.45	4957	2856.54
S10	28 September 2018	0.01–152.72	4337	1866.5

Figure 3. Position of one ROI and one tussock. The point cloud data collected in June 2017 are rendered in a 3D scene from the top view.

rates were classified into four levels (Table 2) with a reference speed of 3.2 cm/mo; this speed was identified in previous work as the monthly depositional rate in the study area (Hu *et al.*, 2019). Both inner and outer boundary profiles were generated from the merged PCD files and DEMs as mentioned previously based on the positions of the vegetation boundary lines.

Vegetation and Topographic Feature Acquisition

The features applied in "Results" included the vegetation area, dense meadow area, area of one cluster (Figure 3), horizontal positions of the inner and outer boundaries, area-level classification of the deposition rate, and profiles of the inner and outer boundaries.

Based on the vegetation points (the green points in Figure 3), the plan points of the inner and outer boundaries were extracted with the Fit tool in the Cloud Compare software (at a 5-m resolution). Then, the plan coordinates of these points were clipped manually to the open curves of both inner and outer boundaries. Meanwhile, the vegetation points were transformed into image coordinates using OpenCV (an open, third-party library) with a 1-pixel resolution of 0.1 m. Then, a connectivity analysis was carried out on these images to classify the vegetation points into different clusters. Among these clusters, dense meadows held the largest area.

Based on these connectivity analyses, the datasets characterizing every two adjacent images were overlapped to judge whether the clusters from one dataset intersect those from another dataset. The seedlings were identified as the remaining clusters that did not intersect in area with clusters from other datasets. The opposite cases were identified as tussocks. Then, the center-point coordinates of each seedling were calculated. With these center points, the distances between seedlings and tussocks were calculated. The average distance

Table 2. *Classification of the deposition rate based on the reference rate of 3.2 cm/mo from a previous study.*

Type	Description
Level 1	Deposition rate is smaller than 3.2 cm/mo
Level 2	Deposition rate is between 3.2 and 6.4 cm/mo
Level 3	the Deposition rate is between 6.4 and 9.6 cm/mo
Level 4	Deposition rate is bigger than 9.6 cm/mo

Table 3. *Classification of the distance between one seedling and other seedlings or tussocks.*

Type	Description
Level 1	Distance is smaller than 5 m
Level 2	Distance is between 5 and 10 m
Level 3	Distance is between 10 and 20 m
Level 4	Distance is between 20 and 30 m
Level 5	Distance is between 30 and 40 m
Level 6	Distance is bigger than 40 m

between each seedling and its six neighboring seedlings was also calculated for further research.

Statistical Analysis

Statistical analyses were carried out to determine the expansion rates of both seedlings and tussocks and the spatial relationship between these vegetation patterns. First, the average distance between one seedling and its neighbors and the distance between each seedling and its nearest tussock were calculated. These distances were categorized into six classes (Table 3). Finally, the expansion widths of both seedlings and tussocks were calculated and classified into one of three types (Table 4) for further study based on the overlapping analysis method mentioned previously.

RESULTS

In this section, the LIDAR data quality is first discussed. Then, the overall change in the vegetation expansion process is described. After that, the different change patterns of seedlings and tussocks are analyzed. Moreover, a spatial analysis between seedlings and tussocks is provided. Finally, the topographic changes and the changes in the vegetation boundary profiles are presented.

Data Quality

The horizontal errors in the acquired data are mainly within 0.02 m, and the vertical errors are mainly within 0.04 m (Figure 4). In this work, when studying vegetation expansion, the horizontal spatial resolution at which vegetation is extracted is 0.1 m. Thus, the data quality is sufficiently reliable for conducting the overlapping analysis. The average accumulation rate was 3.2 cm/mo before 2016 according to a previous study (Hu *et al.*, 2019). Thus, the vertical errors are not sufficient to analyze the monthly deposition change process. However, the data are still sufficiently reliable to analyze the average topographic change trends in the two observation phases.

Vegetation Expansion Process

First, the overall area increased continuously except for a slight decrease from August to September 2018 (Figure 5b). One possible reason for this decrease is that the data collected in September 2018 were acquired following rain; thus, the tidal flat surface held a high moisture content. When scanning areas

Table 4. *Classification of expansion speed into three types based on their width.*

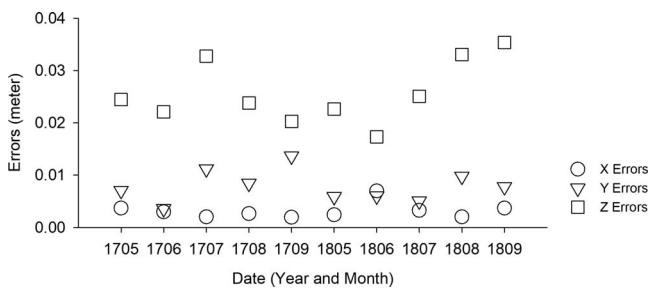| Type	Description
Small	Width is smaller than 1 m
Middle	Width is between 1 and 3 m
Big	Width is bigger than 3 m

Figure 4. The LIDAR data errors in the plan space (circles and triangles) and vertical direction (squares).

with high moisture, the near-infrared laser signal is absorbed or subject to complete specular reflection (Blenkinsopp *et al.*,

2010; Heritage and Hetherington, 2007), thus generating nonvalue areas in the acquired point cloud data. Without considering these data, the increasing processes in the two periods can be divided into two stages: a slow incremental stage and a rapid incremental stage. In 2017, the area increased steadily from 8.36 to 14.49 ha in the first four months and then sharply increased to 28.22 ha, an increment nearly seven times that of the monthly average increment measured in the first stage (approximately 2 ha). In 2018, the area increased steadily from 29.25 to 32.15 ha in the first three months and then sharply increased to 41.24 ha, with an increment of more than six times the monthly average increment measured in the first stage (approximately 1.45 ha).

The change in the dense meadow area also indicated significant stage changes (Figure 5a,b). In 2017, the area remained nearly constant in the first four months, increasing from 3.51 to 4.12 ha, and then increased dramatically to 19.08
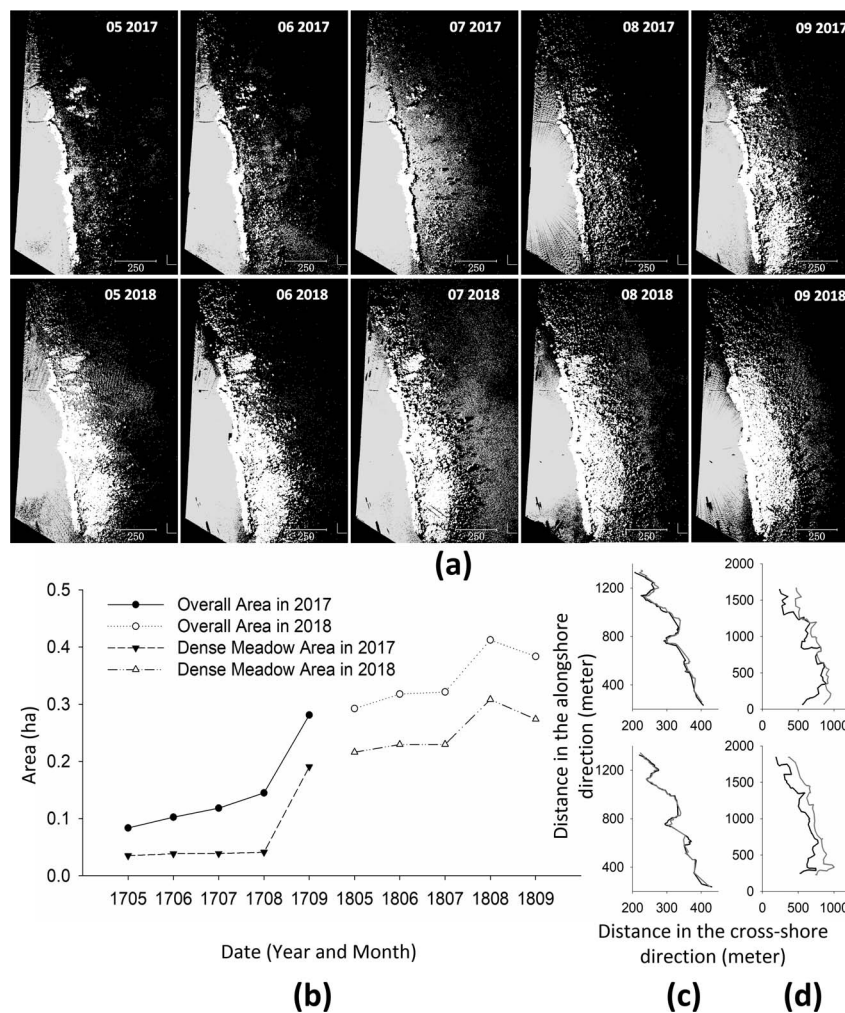
Figure 5. Overall change process of vegetation. (a) The spatial distribution of vegetation in each month is rendered in Cloud Compare software. (b) The area curves of the overall vegetation and dense meadow. (c) The horizontal positions of the inner boundaries in both years; the black lines represent the first month, and the gray lines represent the last month. (d) The horizontal positions of the outer boundaries in both years; the black lines represent the first month, and the gray lines represent the last month.

Figure 6. The seedling and tussock extraction results in the ROI and one tussock from the ROI. (a) The 3D rendered map of seedlings and tussocks in all four periods in both years. (b) The monthly expansion process of one tussock.

ha in September, growing to more than 4.5 times its size measured in August. In 2018, the area increased slightly in the first three months from 21.63 to 22.99 ha and subsequently
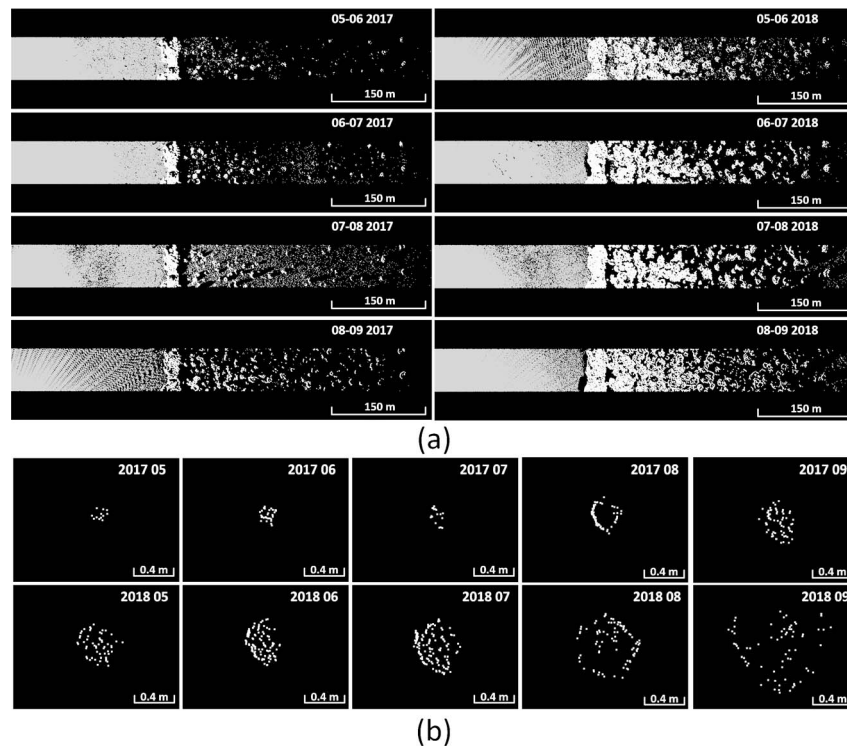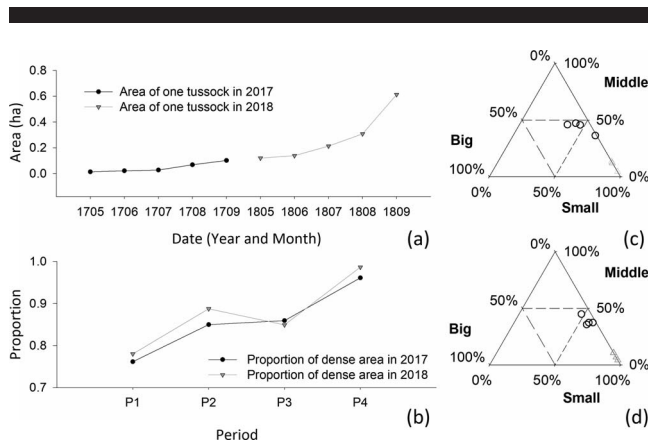

Figure 7. (a) Area change in the tussock shown in Figure 6b. (b) The proportion curves of the dense area from Figure 8a,b, with P1 to P4 representing Period 1 (from May to July) to Period 4 (from August to September). (c) and (d) Classified expansion widths of both seedlings (triangles) and tussocks (circles) of different sizes in 2017 and 2018, respectively. In each ternary plot, the region is roughly divided into four subregions; the lower right subregion represents a small subregion, the upper subregion represents a moderately sized subregion, and the lower left subregion represents a large subregion.

increased dramatically to 30.84 ha in August. The change in the shape of the dense meadows shown in Figure 5a also illustrates the same change pattern. The dense meadow remained nearly unchanged in the first four months; then, the southern part of the dense meadow area suddenly formed a dense expanding area spanning approximately 235 m toward the sea. In the following year, the dense area remained unchanged in the first three months. Then, the dense area expanded northward. The maximum expansion distance was nearly 85 m.

The change processes of the inner and outer boundaries were different from each other (Figure 5c,d). In both phases, the inner boundary barely changed (Figure 5c). The average expansion distances were 6.02 and 3.09 m in 2017 and 2018, respectively. Moreover, the monthly expansion distances were only 1.51 m (in 2017) and 0.77 m (in 2018). However, the outer boundary expanded seaward and northward (Figure 5d) with average expansion distances of 69.76 and 189.18 m, respectively; the maximum expansion distances were 289.12 and 373.05 m and the monthly expansion speeds were 17.44 and 47.30 m/mo, respectively.

Change Patterns of Both Tussock and Seedling

One region of interest (ROI) was selected to reveal the extraction results of tussocks and seedlings in different periods (Figure 6a). Figure 6b shows the expansion process of one tussock from this ROI. The area curve displayed in Figure 7a illustrates that in 2017, the area remained still in the first three months and continued to slightly increase in the last two
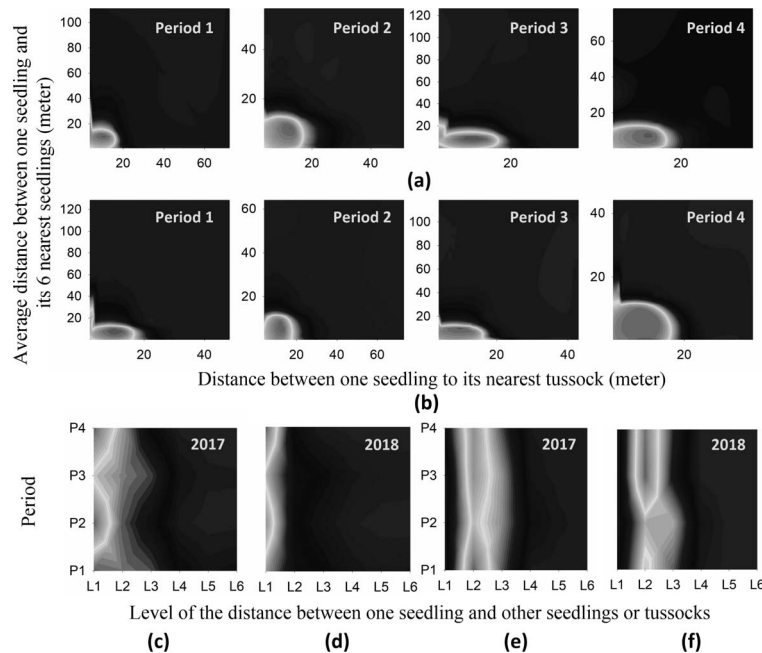
Figure 8. The spatial relationship between seedlings and tussocks. (a) and (b) The spatial relations between the average distance between one seedling and its six nearest seedlings and the distance between one seedling and its nearest tussock in 2017 and 2018, respectively. (c) and (d) Different distances between one seedling and its nearest tussock in 2017 and 2018, respectively. (e) and (f) Different distances between one seedling and its six nearest seedlings in 2017 and 2018, respectively.

months, with an average rate of increase of 0.04 m²/mo. In the following year, the area increased steadily from 0.1201 to 0.3082 m² in the first four months (with an average increment of 0.0627 m²) and increased sharply to 0.6127 m² in the last month, with an increment speed nearly five times that measured before.

Based on their different sizes (Table 4), the expansion widths were classified into three types, as shown in Figure 7c,d. The tussock expansion widths were mainly concentrated in the moderate size (between 1 and 3 m), whereas those of seedlings were mainly concentrated in the small size (less than 1 m).

The spatial analysis shows that the average distance (dis1) between one seedling and its six nearest seedlings was closely related to the distance (dis2) between the seedling and its nearest tussock point (Figure 8a,b). First, a dense area was shown in all phases in both years, with both dis1 and dis2 within 20 m. The percentages of points in this dense area were all larger than 70% and presented an overall increasing trend (Figure 7b).

The distances between seedlings and tussocks were analyzed, and the statistical results are shown as percentages in Figure 8c,d. Based on the high-value areas shown in these two figure panels, these distances were mainly concentrated within Level 3 (L3: in 2017) and Level 2 (L2: in 2018). Two peak values were found in Period 2 (P2: from May to June) and Period 4 (P4: from August to September) in both years within Level 1 (L1). In 2017, the percentage value within L1 increased more than twofold from 25.39 to 56.57%, dropped to 36.66%, and finally increased again to 56.26%. In 2018, a similar change process

was observed within L1. The percentage value increased rapidly from 48.24 to 72.15%, dropped to 52.78%, and finally increased to 84.86%.

The statistical analysis results obtained for the distances between two seedlings are illustrated in Figure 8e,f. Significant concentration zones can be seen in both figures. These zones are between L2 and L3, which together hold the main share in both years. Moreover, the percentage values within L2 hold all peak values in all periods. In 2017, the percentage values at L2 (between L2 and L3) contained 66.11% (94.01%), 49.11% (83.48%), 57.40% (92.91%), and 57.97% (84.51%) of the overall values in the four periods. In 2018, the L2 values (between L2 and L3) represented 52.56% (84.84%), 43.74% (86.85%), 72.13% (93.84%), and 69.36% (95.39%) of the overall points in the four periods.

Topographic Change

By comparing the data collected herein to the average deposition rate obtained from a formal study, the monthly sediment speeds were classified into four levels according to Table 2. A total of 57.88% of the area in 2017 and 69.06% of the area in 2018 experienced faster deposition than that experienced in the same areas before 2016 (Figure 9). The L2 area in 2017 was approximately equal to that in 2018 (Figure 10a). The L3 area in 2018 was nearly twofold that in 2017 (Figure 10a).

The topographic profiles of the inner boundaries (Figure 10b,c) in the first month (black lines) and the last month (red lines) illustrate the depositional change process. In 2017, the average deposition height was 15.8 cm and the average monthly deposition rate was 4 cm, with a maximum rate of 7
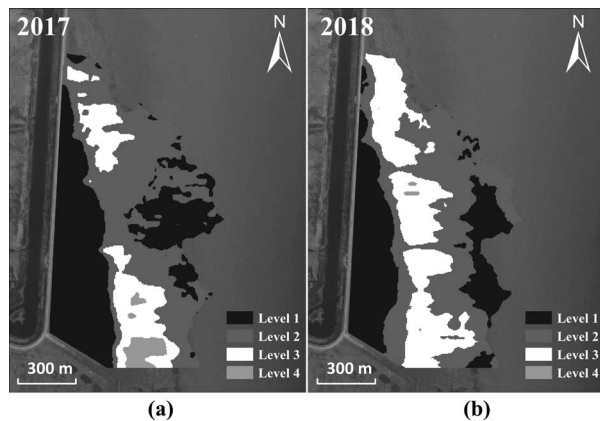
Figure 9. Different deposition rates in the two phases.

cm/mo. In 2018, the average deposition height was 8 cm and the average monthly rate was 2.6 cm, with a maximum rate of 5.2 cm/mo. The mean elevation increased from 3.73 to 3.85 m in 2017 and from 3.87 to 3.94 m in 2018.

The deposition change process data collected at the outer boundaries are presented in Figure 10d,e. In the first year, the average deposition height was 19.2 cm and the average monthly rate was 4.8 cm, with a maximum rate of 10.3 cm/mo. In 2018, the average deposition height was 10 cm and the average monthly rate was 3.3 cm, with a maximum rate of 6.2 cm/mo. The mean elevation increased from 2.23 to 2.42 m in 2017 and from 2.45 to 2.55 m in 2018.

DISCUSSION

In this section, the general vegetation change process is discussed, including both area changes and boundary changes in vegetation. Then, the change patterns of both tussocks and seedlings are studied based on spatial statistical analyses.

General Change Process of Vegetation

The change patterns of vegetation areas were found to have stages in both years of study. The area curves of the overall vegetation zone, the dense meadow area, and one cluster selected from the ROI present two stages in their respective change processes. The increment rate in the second stage is greater than that in the first stage. The turning points between the two stages vary from July to August among these situations.

Different vegetation boundary-expansion processes were observed. The outer boundaries moved forward toward the shoreline in the first year and then expanded northward in the following year. However, the inner boundaries barely changed. One possible reason for this observation might be related to residual chemical herbicides in the soil. The increased scale of *Scirpus* spp. was large at the study site, especially after 2015, when the adjacent *Spartina* was executed through herbicide use. The inner boundary profiles increased in both phases, whereas their corresponding positions changed little. Thus, another possible reason for this observation may be related to the suitable height range for pioneer vegetation. The mean evolution of the inner boundaries reached nearly 4 m, which is beyond the suitable height range of pioneer vegetation (Tao *et al.*, 2017).

Typical positive feedback effects were observed between vegetation colonization and sedimentation accretion. Compared with the monthly sedimentation rate measured before 2016, the deposition rate increased two to four times throughout the study period. Areas with higher deposition rates were mainly found in the vegetation areas and vegetation frontier zones (Figure 9). After equally dividing the study area into northern, middle, and southern subareas, the middle subarea showed significant seaward expansion at L2. At L3 and L4, the northern and southern subareas (in 2017) expanded toward the whole vegetation area (in 2018).

The establishment of pioneer vegetation promotes tidal flat accretion and reduces hydrodynamic energy through sediment trapping and wave attenuation. As the canopy density and marsh elevation increase, vegetation colonization is further improved until an alternative stable state is presented (Mudd, D'Alpaos, and Morris, 2010; Van De Koppel *et al.*, 2001; Vandenbruwaene *et al.*, 2011). However, the topographic changes in the northern subarea, which is located quite close
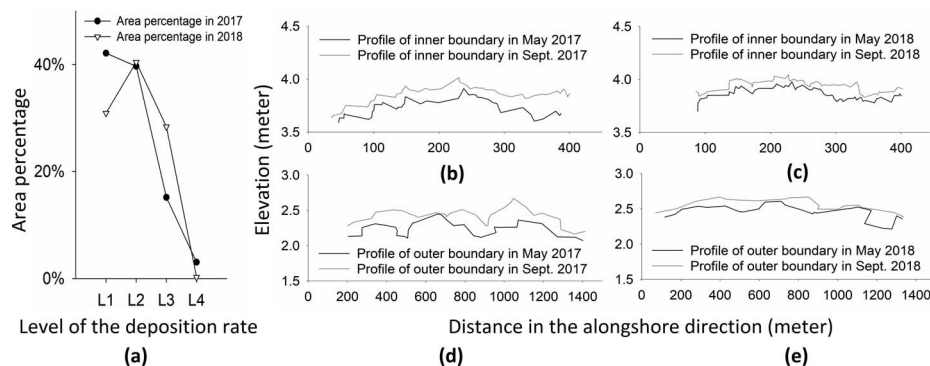
Figure 10. The area percentage curves and profiles of both inner and outer boundaries. (a) The area percentage curves in 2017 and 2018. (b) and (c) The inner vegetation boundary profiles; the black line represents May and the gray line represents September in 2017 and 2018, respectively. (d) and (e) The outer vegetation boundary profiles; the black line represents May and the gray line represents September in 2017 and 2018, respectively.

to the seawall, should be dominated by the effects of the seawall.

Change Patterns of Seedlings and Tussocks

The two modes of expansion identified for seedlings and tussocks showed different trends. The width-expansion speed of tussock development was faster than that of seedling recruitment. According to the classified results (Figure 7c,d), the monthly development of tussocks was concentrated in the moderate size, whereas that of seedling recruitment was mainly concentrated in the small size. Tussock development mainly contributed to the overall increase in the vegetation area. The development of one cluster (Figure 6b) from the ROI indicated that tussocks expanded through the peripheral diffusion mechanism.

A strong spatial relationship was found between tussocks and seedlings. The seedlings were densely concentrated within a certain distance (20 m in this work) from the tussocks (Figure 8a,b); the percentage of points within 20 m of each seedling tended to increase continuously. Moreover, the average distance (Figure 8e,f) between one seedling and its six neighboring seedlings was concentrated from 10 to 20 m. A similar change pattern was observed for the distance between one seedling (Figure 8c,d) and its nearest tussock in both years. In Period 1, the presence of seedlings tended to decrease as their distances to tussocks increased. Then, the seedlings became concentrated within 5 m from tussocks. In the next two periods, the same pattern appeared again. This illustrated that with the increasingly rapid expansion of tussocks, the distances between tussocks and seedlings decreased. Compared with 2017, the seedlings measured in 2018 tended to be more concentrated near tussocks.

Previous work has indicated that seed arrival decreases with the distance from the seed-source area, *i.e.* the salt marsh, resulting in seeds being deposited on mudflats close to the marsh edges (Zhu *et al.*, 2014); this trend was consistent with the results obtained herein.

CONCLUSIONS

TLS technology was used in this work to monitor the monthly change patterns of pioneer vegetation. Overall change process research and spatial analyses of both seedling recruitment and tussock development were conducted in this study.

The pioneer vegetation expanded toward the shoreline in the first year and then colonized northward in the second year. Meanwhile, two incremental stages were observed in the change process in the overall study area, in the dense meadow area, and in one selected tussock. This change process suggested a positive feedback effect between vegetation colonization and sediment accumulation. Colonization accelerated the deposition process at the study site. Meanwhile, the sediment accumulation in the northern subarea, which was located close to the seawall, promoted the colonization of vegetation.

A strong spatial relationship was observed between seedling recruitment and tussock development in this study. Tussocks tended to force seedlings to expand outward by squeezing the established space of the seedlings. Moreover, seedlings were densely concentrated within a certain distance from the tussocks. The distances between seedlings and tussocks tended to shorten annually as the expansion process of the whole vegetation area progressed. The average distances between seedlings were concentrated at 10 to 20 m.

The results of this study demonstrate the potential of using TLS technology to monitor monthly vegetation expansion processes on small and medium scales. The advantages of TLS methods are reflected in the rapid acquisition of data with high resolution and high precision. Moreover, taking into account the sensitivity of near-infrared lasers to water (Blenkinsopp *et al.*, 2010; Heritage and Hetherington, 2007), the TLS data-acquisition process should avoid collection situations similar to the rainy conditions that occurred in September 2018 in this work. Finally, the laser may not be able to penetrate vegetation (Lei *et al.*, 2014). In this work, the vegetation was low; thus, one fixed scanning station was sufficient to acquire vegetation data. For higher vegetation, multiple stations should be applied to scan the scene from various angles.

LITERATURE CITED

Balke, T.; Klaassen, P.C.; Garbutt, A.; Van der Wal, D.; Herman, P.M., and Bouma, T.J., 2012. Conditional outcome of ecosystem engineering: A case study on tussocks of the salt marsh pioneer *Spartina anglica*. *Geomorphology,* 153, 232–238.

Blenkinsopp, C.E.; Mole, M.A.; Turner, I.L., and Peirson, W.L., 2010. Measurements of the time-varying free-surface profile across the swash zone obtained using an industrial LIDAR. *Coastal Engineering,* 57(11–12), 1059–1065.

Bouma, T.J.; Van Belzen, J.; Balke, T.; Van Dalen, J.; Klaassen, P.; Hartog, A.M., and Herman, P.M.J., 2016. Short-term mudflat dynamics drive long-term cyclic salt marsh dynamics. *Limnology and Oceanography,* 61(6), 2261–2275.

Chen, W. and Temmerman, S., 2013. Does biogeomorphic feedback lead to abrupt shifts between alternative landscape states? An empirical study on intertidal flats and marshes. *Journal of Geophysical Research: Earth Surface,* 118(1), 229–240.

CloudCompare. 3D point cloud and mesh processing software: Open source project. https://www.cloudcompare.org/

Donatelli, C.; Ganju, N.K.; Zhang, X.; Fagherazzi, S., and Leonardi, N., 2018. Salt marsh loss affects tides and the sediment budget in shallow bays. *Journal of Geophysical Research: Earth Surface,* 123(10), 2647–2662.

Duarte, C.M.; Middelburg, J.J., and Caraco, N., 2005. Major role of marine vegetation on the oceanic carbon cycle. *Biogeosciences,* 2(1), 1–8.

Fagherazzi, S.; Kirwan, M.L.; Mudd, S.M.; Guntenspergen, G.R.; Temmerman, S.; D'Alpaos, A., and Clough, J., 2012. Numerical models of salt marsh evolution: Ecological, geomorphic, and climatic factors. *Reviews of Geophysics,* 50(1), RG1002.

Ferronato, C.; Speranza, M.; Ferroni, L.; Buscaroli, A.; Vianello, G., and Antisari, L.V., 2018. Vegetation response to soil salinity and waterlogging in three saltmarsh hydrosequences through macronutrients distribution. *Estuarine, Coastal and Shelf Science,* 200, 131–140.

Fey, C.; Schattan, P.; Helfricht, K., and Schöber, J., 2019. A compilation of multitemporal TLS snow depth distribution maps

at the Weisssee snow research site (Kaunertal, Austria). *Water Resources Research,* 55(6), 5154–5164.

Ganju, N.K.; Defne, Z.; Kirwan, M.L.; Fagherazzi, S.; D'Alpaos, A., and Carniello, L., 2017. Spatially integrative metrics reveal hidden vulnerability of microtidal salt marshes. *Nature Communications,* 8(1), 1–7.

Ge, Z.M.; Cao, H.B.; Cui, L.F.; Zhao, B., and Zhang, L.Q., 2015. Future vegetation patterns and primary production in the coastal wetlands of East China under sea level rise, sediment reduction, and saltwater intrusion. *Journal of Geophysical Research: Biogeosciences,* 120(10), 1923–1940.

Chen, J.Y. and Yang, Q.I., 1988. *Report of Shanghai Coastal Comprehensive Investigation*. Shanghai, China: Shanghai Scientific and Technological Press, 390p.

Guarnieri, A.; Vettore, A.; Pirotti, F.; Menenti, M., and Marani, M., 2009. Retrieval of small-relief marsh morphology from terrestrial laser scanner, optimal spatial filtering, and laser return intensity. *Geomorphology,* 113(1–2), 12–20.

Heritage, G. and Hetherington, D., 2007. Towards a protocol for laser scanning in fluvial geomorphology. *Earth Surface Processes and Landforms: Journal of the British Geomorphological Research Group,* 32(1), 66–74.

Hladik, C.; Schalles, J., and Alber, M., 2013. Salt marsh elevation and habitat mapping using hyperspectral and LIDAR data. *Remote Sensing of Environment,* 139, 318–330.

Hu, M.Y.; Ge, Z.M.; Li, Y.L.; Li, S.H.; Tan, L.S.; Xie, L.N., and Li, X.Z., 2019. Do short-term increases in river and sediment discharge determine the dynamics of coastal mudflat and vegetation in the Yangtze Estuary? *Estuarine, Coastal and Shelf Science,* 220, 176–184.

Hu, Z.J.; Ge, Z.M.; Ma, Q.; Zhang, Z.T.; Tang, C.D.; Cao, H.B., and Zhang, L.Q., 2015. Revegetation of a native species in a newly formed tidal marsh under varying hydrological conditions and planting densities in the Yangtze Estuary. *Ecological Engineering,* 83, 354–363.

Huang, H.M. and Zhang, L.Q., 2007. The spatio-temporal dynamics of salt marsh vegetation for Chongming Dongtan National Nature Reserve, Shanghai. *Acta Ecologica Sinica,* 27(10), 4166–4172.

Hulzen, J. and Bouma, J.J., 2007. Morphological variation and habitat modification are strongly correlated for the autogenic ecosystem engineer *Spartina anglica* (common cordgrass). *Estuaries & Coasts,* 30(1), 3–11.

Kirwan, M.L. and Megonigal, J.P., 2013. Tidal wetland stability in the face of human impacts and sea-level rise. *Nature,* 504(7478), 53–60.

Lee, T.M. and Yeh, H.C., 2009. Applying remote sensing techniques to monitor shifting wetland vegetation: A case study of Danshui River estuary mangrove communities, Taiwan. *Ecological Engineering,* 35(4), 487–496.

Lei, F.; Powrie, W.; Smethurst, J.; Atkinson, P.M., and Einstein, H., 2014. The effect of short ground vegetation on terrestrial laser scans at a local scale. *ISPRS Journal of Photogrammetry and Remote Sensing,* 95(3), 42–52.

Marani, M.; Belluco, E.; Ferrari, S.; Silvestri, S.; D'Alpaos, A.; Lanzoni, S., and Rinaldo, A., 2006. Analysis, synthesis and modelling of high-resolution observations of salt-marsh eco-geomorphological patterns in the Venice lagoon. *Estuarine, Coastal and Shelf Science,* 69(3–4), 414–426.

Mudd, S.M.; D'Alpaos, A., and Morris, J.T., 2010. How does vegetation affect sedimentation on tidal marshes? Investigating particle capture and hydrodynamic controls on biologically mediated sedimentation. *Journal of Geophysical Research: Earth Surface,* 115(F3), F03029.

Nehring, S. and Hesse, K.J., 2008. Invasive alien plants in marine protected areas: The *Spartina anglica* affair in the European Wadden Sea. *Biological Invasions,* 10(6), 937–950.

Point Cloud Library. https://pointclouds.org/

Sadro, S.; Gastil-Buhl, M., and Melack, J., 2007. Characterizing patterns of plant distribution in a southern California salt marsh using remotely sensed topographic and hyperspectral data and local tidal fluctuations. *Remote Sensing of Environment,* 110(2), 226–239.

Silvestri, S.; Marani, M., and Marani, A., 2003. Hyperspectral remote sensing of salt marsh vegetation, morphology and soil topography. *Physics & Chemistry of the Earth Parts A/B/C,* 28(1–3), 15–25.

Suchrow, S. and Jensen, K., 2010. Plant species responses to an elevational gradient in German North Sea salt marshes. *Wetlands,* 30(4), 735–746.

Tao, Y.; Yu, K.; He, P.; Sun, B., and Fang, S., 2017. Distribution of *Scirpus mariqueter* on Nanhui coasts after reclamation and the associated affecting factors. *Resources and Environment in the Yangtze Basin,* 26(7), 1032–1041.

Thiebes, B.; Wang, J.; Bai, S., and Li, J., 2013. Terrestrial laser-scanning of tidal flats—a case study in Jiangsu Province, China. *Journal of Coastal Conservation,* 17(4), 813–823.

Van De Koppel, J.; Herman, P.; Thoolen, P., and Heip, C., 2001. Do alternate stable states occur in natural ecosystems? Evidence from a tidal flat. *Ecology,* 82(12), 3449–3461.

Vandenbruwaene, W.; Temmerman, S.; Bouma, T.J.; Klaassen, P.C., and Meire, P., 2011. Flow interaction with dynamic vegetation patches: Implications for biogeomorphic evolution of a tidal landscape. *Journal of Geophysical Research: Earth Surface,* 116(F1), F01008.

Xie, W.; Guo, L.; Wang, X.; He, Q., and Yu, X., 2021. Detection of seasonal changes in vegetation and morphology on coastal salt marshes using terrestrial laser scanning. *Geomorphology,* 380(1), 107621.

Xie, W.; He, Q.; Zhang, K.; Guo, L.; Wang, X.; Shen, J., and Cui, Z., 2017. Application of terrestrial laser scanner on tidal flat morphology at a typhoon event timescale. *Geomorphology,* 292, 47–58.

Yuan, L. and Zhang, L.Q., 2008. Mapping large-scale distribution of submerged aquatic vegetation coverage using remote sensing. *Ecological Informatics,* 3(3), 245–251.

Zedler, J.B. and Kercher, S., 2005. Wetland resources: Status, trends, ecosystem services, and restorability. *Annual Review of Environment & Resources,* 15(30), 39–74.

Zhu, Z.; Bouma, T.J.; Ysebaert, T.; Zhang, L., and Herman, P., 2014. Seed arrival and persistence at the tidal mudflat: Identifying key processes for pioneer seedling establishment in salt marshes. *Marine Ecology Progress Series,* 513, 97–109.

Zhu, Z.; Zhang, L.; Wang, N.; Schwarz, C., and Ysebaert, T., 2012. Interactions between the range expansion of saltmarsh vegetation and hydrodynamic regimes in the Yangtze Estuary, China. *Estuarine Coastal & Shelf Science,* 96, 273–279.